# Wing Force Map Characterization and Simulation for the Micromechanical Flying Insect

Joseph Yan
Department of ECE
University of British Columbia
Vancouver, BC, Canada  V6T 1Z4

Ronald S. Fearing
Dept of EECS
University of California, Berkeley
Berkeley, CA  94720, USA

*Abstract*— The first force map has been generated for a 2 DOF wing designed for the MFI project. For the wing beating at a resonance frequency of 139 Hz, the average 3-D forces were found as a function of sinusoidal voltage amplitude and actuator phase difference. An image sequence of the wing trajectory allowed comparison to simulated forces using a quasi-steady state aerodynamic approximation. Finally, the results were compared to the case of ideally matched leading/lagging wing dynamics driven by sinusoids.

## I. Introduction

Many micro aerial vehicle (MAV) developers have opted for fixed wing or rotary wing aircraft designs but most analysts agree that the best solutions to building smaller MAVs closer to the centimeter-scale may be inspired from nature (*i.e.*, a biomimetic MAV, or BMAV). Biological flying insects use flapping wings to attain amazing capabilities for hovering and maneuvering. Most of the recent work on BMAVs has been on the scale of avian flight which is quite different from insect flight. Notable examples in this list include the Vanderbilt MAV (Cox *et al* [2]), the Caltech/UCLA Ornithopter (Pornsin-Sirirak *et al* [5]), and the Georgia Tech Entomopter (Michelson and Reece [4]).

The UC Berkeley Micromechanical Flying Insect (MFI) is a BMAV under development which distinguishes itself with a wingspan of only 25 mm, almost an order of magnitude smaller than all the others (this translates into roughly three orders of magnitude difference in mass). Previous work on the MFI has been documented in a number of areas including design and fabrication (Yan *et al* [12]), actuator development (Sitti *et al* [9]), thorax dynamics (Avadhanula *et al* [1]), sensing (Wood *et al* [10]) and aerodynamic simulation (Schenato *et al* [8]).

The success of insect-scale BMAVs depends on exploitation of unsteady aerodynamic mechanisms (in particular, *delayed stall, rotational lift*, and *wake capture*) which have only recently been elucidated by Dickinson *et al* [3]. There has been some success with computational methods to estimate forces generated by flapping wings [6] but both the models and algorithms need to be improved in order to get better agreement with experimental values. The only reliable means to determine the forces generated by the flapping wing is to measure them directly. Comparisons can then be made to validate, improve, or dismiss other methods of force estimation.

This paper describes the first force map characterization for a specific 2-DOF thorax driven at resonance. The mapping relates input voltage amplitudes and phase difference to the lift, thrust, and lateral forces generated by the wing. The results are compared to estimated forces based on an image sequence of the wing and quasi-steady state aerodynamic models.

## II. Force Map Generation

Understanding the forces generated while the wing is beating is important to carrying out control. Forces can be estimated using quasi-steady aerodynamic models which rely on ideal kinematics or they may be extrapolated from experimental data taken with dynamically-scaled models (*e.g.*, using the Robofly apparatus of [3]). These estimates may provide qualitative information about the forces but the quantitative values often do not agree with experimental values so the wing forces need to be measured directly.

### A. Experimental Setup

Ideally, a multi-axis sensor could be used to measure the forces/moments for all six axes (most importantly, along the lift and thrust directions). Furthermore, the sensor would have sufficient resolution to determine the net forces averaged over periodic wing motion. Sensors based on strain gauge technology have previously been used for measuring MFI instantaneous wing forces [10]; however, the sensor range was designed to accommodate the wing inertial forces which dwarf the net aerodynamic forces (instantaneous wing inertial forces as high as 10 mN can be expected while estimates of net forces were less than 100 $\mu$N; the sensor resolution was on the order of 10 $\mu$N). Another sensor was needed which did not require high bandwidth but could measure the mean wing forces with adequate resolution (1 $\mu$N was deemed reasonable). Several attempts were made to build such a sensor, first using strain gauges, then a commercial linear variable differential transformer (LVDT), and finally a capacitive sensor. Unfortunately, the strain gauges exhibited unacceptable drift while the experimental setups for both the LVDT and capacitive sensors required tedious calibration.

Furthermore, none of these methods could readily be adapted to measure the force simultaneously along more than one axis.

Ultimately, a commercial precision balance was used to collect the force data, a single axis at a time. The AND HR-60 is accurate to 0.1 mg and has a settling time of 2.5 seconds. Measurements for three orthogonal directions of force were made by mounting the thorax in the orientations shown in Figure 1.
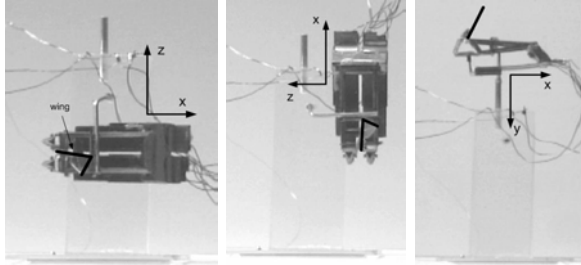


Fig. 1. Thorax mounting for measuring (a) Lift, (b) Thrust and (c) Lateral forces. The leading and distal edges of the transparent wing have been highlighted to make it more noticeable.

### B. 02θ Experimental Force Map

The first thorax for which a force map has been generated is the 2 DOF prototype, designated 02θ. Even before initial operation, some difficult repairs needed to be performed leading to concern that performance would be poor. However, thorax characterization demonstrated that the resonant frequency is 139 Hz (close to the desired specification of 150 Hz), the wing flapping gain is reasonably good at roughly $1.4°/V$, and the thorax survived over 3 hours of operation, with a nominal stroke amplitude of $90°$.

Driving the actuators in phase with a sinusoidal voltage from 0-60 V, the frequency was swept between 100 Hz and 180 Hz to generate the graph in Figure 2. In this range, the lift force was as low as 23 $\mu$N for 100 Hz and as high as 120 $\mu$N for 140 Hz (note that with matched leading and lagging systems and no phase difference between actuation signals, the expected motion is pure flapping which would not generate any lift; the experimentally observed nontrivial force is due to asymmetry in the differential giving rise to excitation of the rotational mode).

Restricting the driving inputs to sinusoids at the resonant frequency for each of the two actuators, there are 5 parameters which may be varied for the characterization: two offset voltages for each actuator, two actuator peak-to-peak voltage amplitudes ($V_{pk-pk}$), and the phase difference between the sinusoids. An exhaustive test of all these parameters would take a considerable amount of time and it is quite possible that the performance would degrade with extended usage, making it difficult to correlate some of the data. Bearing in mind the limited lifetime of each
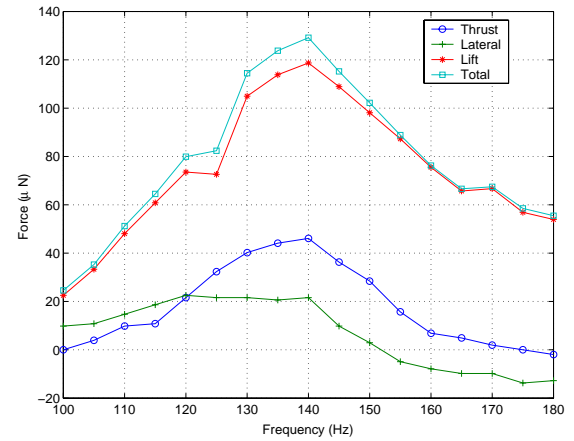


Fig. 2. Measured forces during frequency sweep for actuator driving voltages 0-60 V, in phase.

thorax, a less comprehensive force map was generated by only varying two parameters: (a) phase and (b) $V_{pk-pk}$ (a single amplitude was set for both actuators and voltage offsets were added so that the lowest voltage applied is 0 V to prevent depolarization of the piezoelectric actuator). The phase was varied between $-60°$ to $60°$ (in increments of $20°$ while $V_{pk-pk}$ was varied from 12 V to 84 V (in increments of 12 V). The coarse force maps generated for lift and thrust are shown in Figures 3 and 4, respectively. For the highest voltage amplitude tested (84 V), varying the phase resulted in lift forces ranging from $135\mu$N to $169\mu$N, thrust forces from $20\mu$N to $59\mu$N, and lateral forces from $-14\mu$N to $16\mu$N (graph not shown). Observation of the wing dynamics reveals that there is too much coupling between the leading and lagging spars and it is expected that with better decoupling, the force variation range can be made greater.

For this particular thorax, the force maps also suggest how the model might be reoriented. For example, with $V_{pk-pk}$=84 V, observe that the thrust force is only positive so that hovering wouldn't be possible by just varying the phase. If instead, the mounting is done such that, with zero phase, the force vector is pointing vertically (thorax is inclined backwards at $14.3°$), then both hovering and backwards motion would also be possible. The resulting lift and thrust force maps would change into those shown in Figure 5. Notice that at 84 V, the maximum total lift force is higher and the thrust force has more point symmetry.

In retrospect, more care should also have been taken to try to ensure the actuators were in phase as it is possible that the resonance of one side of the 4-bar was far too dominant. Unfortunately, this prototype has been damaged so more comprehensive testing is not possible without a repair which would likely change some of the dynamic parameters and necessitate a new force map.
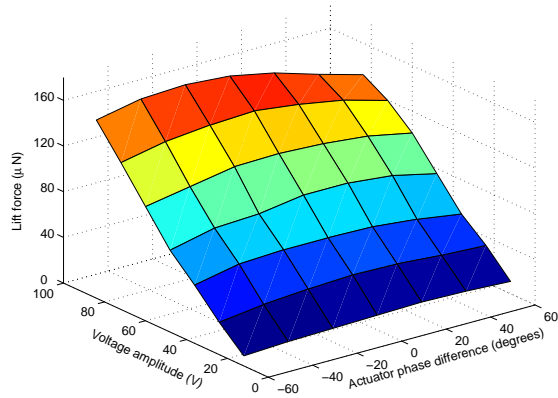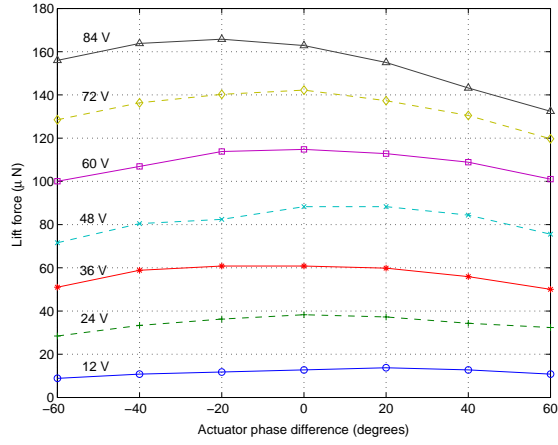
Fig. 3.   Lift Force maps for operation at nominal $139Hz$.



Fig. 4.   Thrust Force maps for operation at nominal $139Hz$.

## III. FORCE SIMULATION

Using infinitesimal wing blade elements and quasi-steady state aerodynamic approximations based on periodic wing motion (see Sane and Dickinson [7] and Schenato *et al* [8]), the expected wing forces can be calculated. These estimates account for contributions from the wing translational and rotational motions but not yet wake capture. For the wing shown in Figure 6, the instantaneous differential force contributions from a vertical wing blade element of thickness d$r$ at a distance $r$ from the wing pivot are given as follows:

$$dF_{\text{tr,N}}(t,r) = \frac{1}{2}C_N(\phi_r(t))\rho c(r)U^2(t,r)dr \quad (1)$$

$$dF_{\text{tr,T}}(t,r) = \frac{1}{2}C_T(\phi_r(t))\rho c(r)U^2(t,r)dr \quad (2)$$

$$dF_{\text{rot,N}}(t,r) = C_{rot}\rho c^2(r)\dot{\phi}_r U(t,r)dr \quad (3)$$

where the "tr" and "rot" subscripts indicate whether the contribution is due to translational or rotational motion, the "N" and "T" subscripts indicate that the direction is either normal or tangential to the wing (notice that the rotational component is always assumed as a normal pressure force),
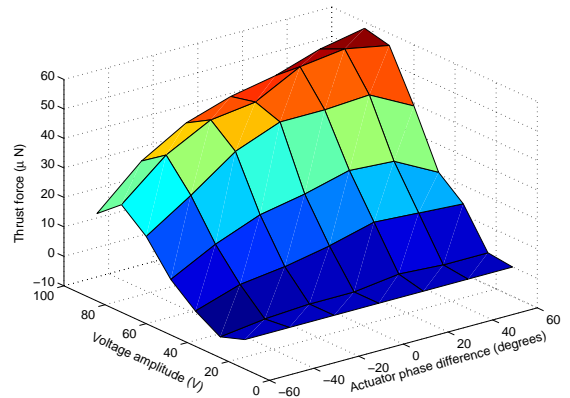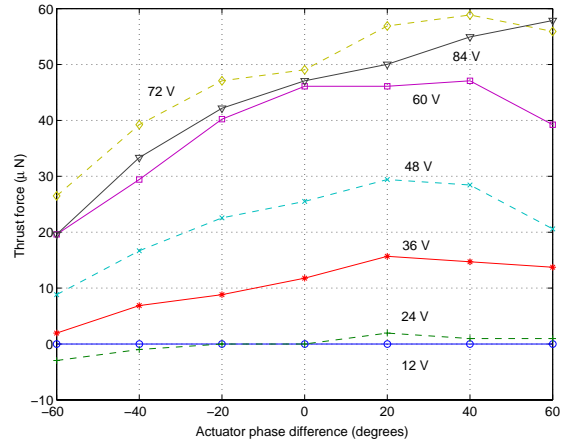
$\rho$ is the density of air, $\phi_r$ and $\phi_f$ are the wing rotation and flapping angles, $U$ is the velocity of the blade element, $c$ is the wing chord width, $C_N$ and $C_T$ are dimensionless translational force coefficients (both are functions of $\phi_r$), and $C_{rot}$ is the rotational force coefficient. $C_{rot}$ is taken to be a function of the non-dimensional axis of rotation $\hat{x}_0$ which varies linearly from zero at the leading edge to unity at the trailing edge:

$$C_{rot} = \pi \left( \frac{3}{4} - \hat{x}_0(r) \right) \quad (4)$$

It is important to note here that $\hat{x}_0$ is conventionally taken to be a constant but this does not adequately consider how the position of the blade element relative to the rotation axis changes the force so it has been written here explicitly as a function of $r$.

### A. Comparison of Experimental Force to Simulated Force from Image Sequence

In the setup of Section II-B, the body is stationary so this simplifies the force estimate as there are no body dynamics to consider. Setting $U(t,r) = \dot{\phi}_f(t)r$, equations
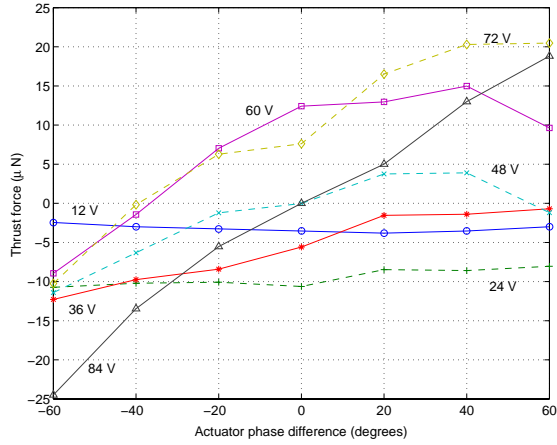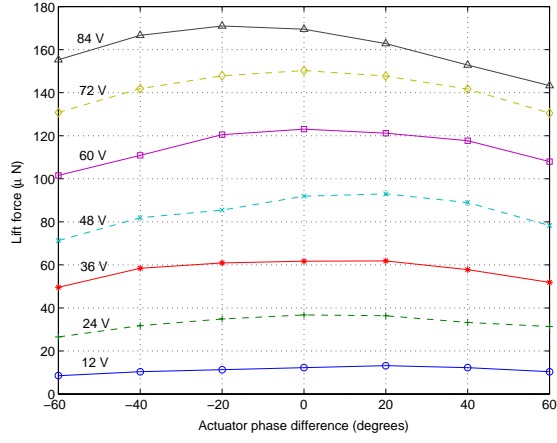
Fig. 5. Predicted (a) lift and (b) thrust force maps for model inclined at 14.3°.

(1)-(3) can be integrated:

$$F_{tr,N}(t) = \frac{\rho C_N(\phi_r(t))\dot{\phi}_f^2(t)}{2}I \tag{5}$$

$$F_{tr,T}(t) = \frac{\rho C_T(\phi_r(t))\dot{\phi}_f^2(t)}{2}I \tag{6}$$

$$F_{rot,N}(t) = \rho\pi\dot{\phi}_r(t)\dot{\phi}_f(t)\tilde{I} \tag{7}$$

where $I$ is the second moment of area of the wing about axis $\mathbf{A}$ and $\tilde{I}$ is a "pseudo area moment":

$$\tilde{I} = \int \left(\frac{3}{4} - \hat{x}_0(r)\right) c^2(r)r\mathrm{d}r \tag{8}$$

The wing of Figure 6 has center of area located at $(x_{ca}, y_{ca}) = (6.70, -1.49)$ mm and the chord length is parameterized according to the equation:

$$c(r) = \begin{cases} \frac{2}{5}r + \frac{4}{5} \text{ mm} & \text{if 3 mm } \leq r < \text{ 8 mm} \\ \frac{4}{3}r + 14\frac{2}{3} \text{ mm} & \text{if 8 mm } \leq r \leq \text{ 11 mm} \\ 0 & \text{otherwise} \end{cases} \tag{9}$$
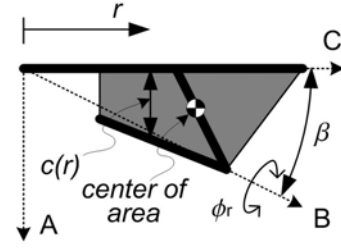


Fig. 6. Wing shape.

For this wing, $I=1020$ mm$^4$ but the calculation for $\tilde{I}$ requires a little more explanation. The experimental Robofly force coefficients of rotation from [7] were computed for a wing with a horizontal rotation axis and the data was only collected for $\hat{x}_0 < 0.75$ so that $C_{rot} > 0$. For the $02\theta$ wing, the axis of *pure* rotation, indicated by the vector $\mathbf{B}$, is dependent on the wing differential morphology (by coincidence this axis also passes through one corner of the distal edge of the wing; the leading edge corresponds to $\mathbf{C}$ and the axis of flapping corresponds to $\mathbf{A}$). Using $\mathbf{B}$ as the axis of rotation, much of the wing will have $\hat{x}_0 > 0.75$ and the net result is that $\tilde{I}$=-140 mm$^4$. The validity of extrapolating using the Robofly data in this case is questionable due to these two fundamental problems: (a) the rotation axis for the MFI wing is at an angle of 26° from the horizontal and (b) the resulting rotation coefficient will be negative, a regime for which there is no Robofly data. One further note is that, using this method, $\phi_f$ should be measured as the flapping angle of $\mathbf{B}$ about the axis defined by $\mathbf{A}$ (this is in contrast to using the axis passing through the center of area, which is arguably a more reasonable choice).

For an image sequence of wing positions such as the one shown in Figure 7, wing features allow determination of the wing orientation at different points in the wing beat cycle. Using a sequence with 18 images for a complete cycle, the resulting stroke and rotation angles were each approximated with a 4-term Fourier series which could be differentiated to give angular velocities (see Figures 8 and 9(a)). The resulting instantaneous force contributions from wing translation and rotation were calculated and plotted in Figure 9 along with the "lift" and "thrust" forces. These instantaneous forces may be more easily visualized in Figure 10 which shows a wing chord and the force acting upon it at several instants in time. It is clear from this figure that the wing motion is far from ideal (wing rotations are too slow and occur too early in the stroke).

The calculated mean lift and thrust forces are 72.5 $\mu$N and 87.3 $\mu$N, respectively. These should be compared to the measured lift and thrust forces of 166 $\mu$N and 42 $\mu$N ($02\theta$ operating at 139 Hz, 0-84 V, 0° phase
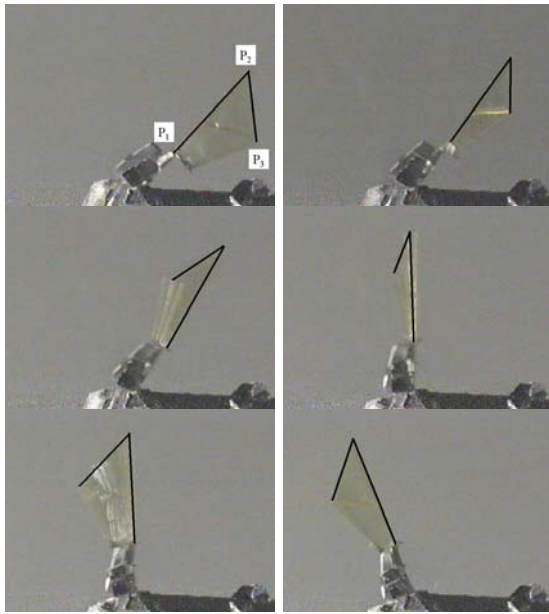
Fig. 7. Clockwise sequence of the periodic wing trajectory with leading and distal edges darkened for easier viewing.
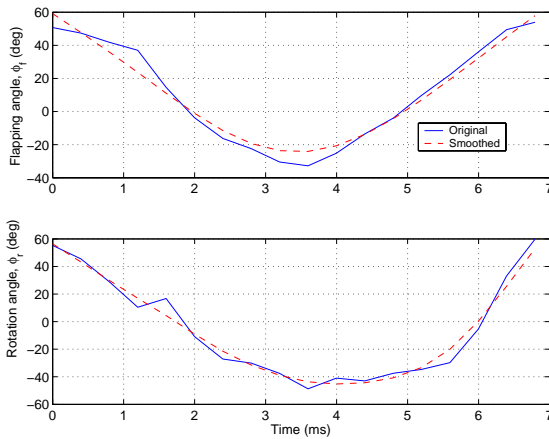


Fig. 8. Using **B** as the rotation axis, the measured (a) stroke flapping and (b) rotation angles were each fitted with a 4-term Fourier series.



Fig. 9. The calculated angular velocities are based on the Fourier approximations. (b) The instantaneous force contributions are calculated using equations (5)-(7). (c) Accounting for the wing rotation angle, the instantaneous lift and thrust forces can be determined.



Fig. 10. Images of a wing chord at various instants in time during the downstroke and upstroke. The circle denotes the leading edge. The arrows show the instantaneous forces acting at the center of area (arrow length is proportional to magnitude).

difference between actuators). In addition to the previous potential problems discussed about extrapolating from Robofly data, there are a number of possible explanations for the discrepancy. Firstly, wake capture can have a significant effect but has not been included in the simulation; this problem is especially relevant to the sequence considered because the stroke amplitude is relatively small which effectively makes the wake capture phenomenon proportionally larger compared to delayed stall. Secondly, the image sequence was not recorded with the intent to determine instantaneous wing positions and some important features in some images were difficult to locate (note the blur of the lea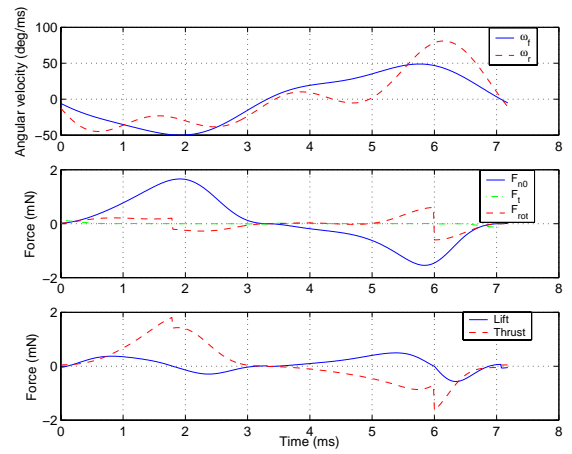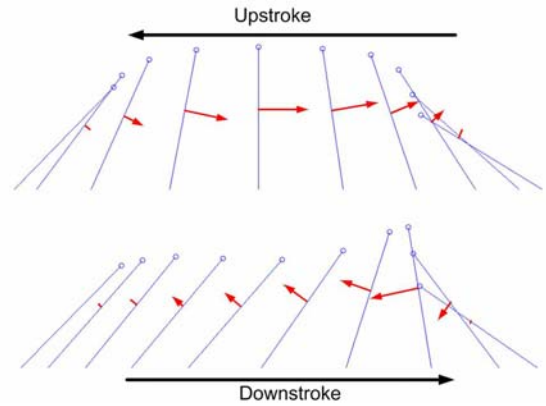ding edge of the third image of the clockwise sequence in Figure 7). A third problem is that the dynamic motion for this thorax is quite far from ideal with a fair bit of wing rotation occurring too early in the stroke. For example, $\phi_r$ switches polarity only a little more than halfway through the upstroke and this may effectively change which edge should be regarded as the "leading" one. The calculations assume a more well-behaved trajectory in which the leading edge stays the same throughout the wing cycle. Fourthly, the stroke and rotation trajectories were fitted with a 4-term Fourier series which will smooth out high frequency components although this is not expected to be a significant problem. Finally, the average force can be drowned out somewhat from the magnitude of the forces. For example, the average estimated thrust force of 87.3 $\mu$N is only 4.8% the value of the maximum instantaneous thrust force of 1.81 mN.

## B. Simulated Force from Image Sequence Using Center of Area to Define Axis of Rotation

One of the problems noted in Section III-A is that the wing differential morphology results in a pure axis of rotation which leads to a negative rotational force coefficient. A reasonable alternative to consider as the rotation axis is the one passing through the wing pivot and the center of area. If the small deviations of this axis from the horizontal stroke plane are negligible, then the same equations could be used. The effective rotational force coefficient is positive ($\tilde{I}$=94.9 mm$^4$). Using the same image sequence of Figure 7, the new flapping angle trajectory $\phi_f(t)$ was computed ($\phi_r(t)$ remains identical) and has a similar shape as before except with a reduced range of -30° to 50°.

The resulting mean lift and thrust forces are 74.3 $\mu$N and 69.8 $\mu$N, respectively. Although both of these values are marginally closer to the experimental values, there is insufficient data to conclude that the calculation with this rotation axis is more appropriate than the one used in Section III-A but it does show that further investigation is necessary.

## C. Simulated Forces Using Ideally Matched Leading/Lagging Dynamics Driven by Sinusoids

It is instructive to consider an ideal case in which the actuator motions can be driven sinusoidally and see how variation of the phase between the actuators changes performance. The complete set of $02\theta$ thorax parameters needed to carry out the idealized calculations in this section is documented in [11] but is not included here due to space constraints.

By varying the *temporal* phase between the two output link sinusoidal motions, the mean lift and thrust forces could be altered as shown in Figure 11. With a phase difference of 0°, the wing motion is purely flapping so, as expected, the lift force is zero and the net thrust force is also zero (the thrust during the upstroke will completely cancel out the thrust during the downstroke). The mean thrust does not exceed 9$\mu$N and is always positive (in the figure, the ripple appears to be an artifact of the method of computation). The maximum lift force of 378 $\mu$N occurs when the lagging actuator is driven 23° behind the leading actuator. The corresponding flapping and rotation angles and their angular velocities are shown in Figure 12. The resulting instantaneous force estimates are shown in Figure 13 and the corresponding chord trajectory is shown in Figure 14.

The maximum simulated mean lift force of 378 $\mu$N is more than double the maximum measured value from the force map but even with two wings, the total lift force would only be 756 $\mu$N which would still be insufficient for takeoff with a mass of 100 mg. With better models that include the effect of wake capture, this may increase
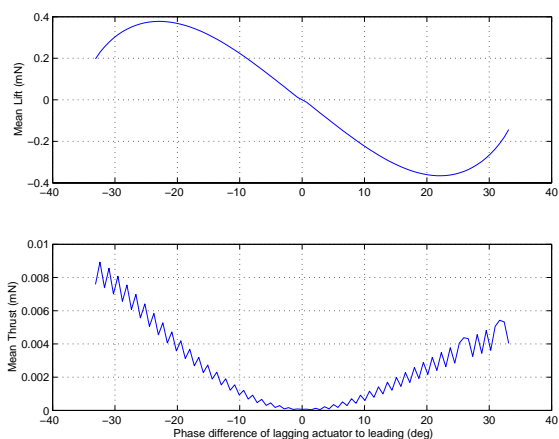


Fig. 11. Simulated variation of mean lift and thrust forces with phase difference between actuator sinusoidal motions.
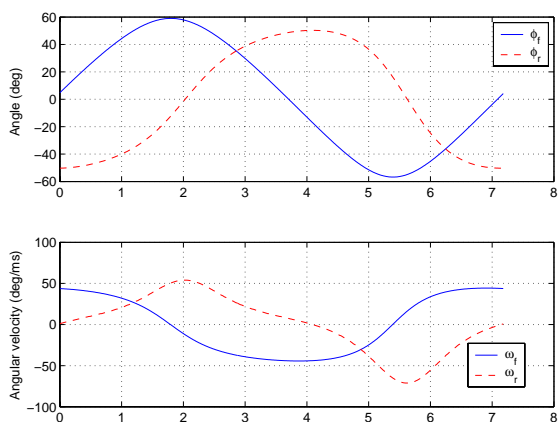


Fig. 12. Simulated (a) flapping and rotation angles and (b) flapping and rotation angular velocities for maximum mean lift force.
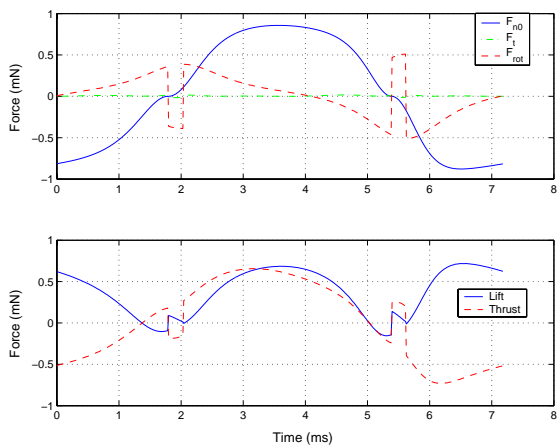


Fig. 13. Simulated (a) instantaneous force contributions for maximum mean lift force using equations (5)-(7). (b) The resulting instantaneous lift and thrust forces.

by at least a factor of two (note that the measured mean lift force is more than double the simulated value using
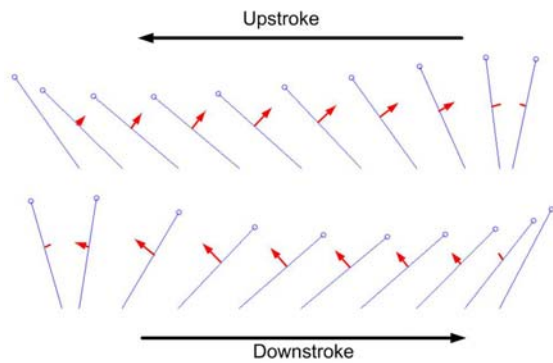
Fig. 14. Images of instantaneous wing chord positions and forces for maximum mean lift force, ideal model.

the observed trajectory). One easy way to increase the lift force would be to increase the amplitude (due to 4-bar kinematic constraints, there are limits to changing this). For example, increasing the actuator voltage amplitude from 84 V to 100 V, the maximum mean lift force increases to $694\mu$N and occurs when the lagging actuator trails the leading one by $18°$ (the flapping angle amplitude goes up from $115.8°$ to $160.6°$ due to nonlinearities). Since the force calculations assume a square dependence on velocity, increasing the frequency from 139 Hz to 150 Hz will cause a 16% improvement in mean lift force.

As observed in Figure 11(b), the simulated mean thrust force cannot be altered much by changing the phase between actuators. This is primarily due to the mostly symmetric nature of the thrust forces during the upstroke and downstroke. Ultimately, this points to the need to be able to drive the actuators with motions other than sinusoids. Two trajectory changes which should prove beneficial are the ability to adjust the ratio of downstroke duration to upstroke duration (the downstroke for biological flying insects is typically faster than the upstroke) and the capability to execute more rapid wing rotations at the end of each stroke.

## IV. DISCUSSION

The first force map has been generated for a 2 DOF MFI wing. The experimental setup was somewhat tedious and points to the need to develop a multi-axis force sensor with high resolution ($\approx 1$ $\mu$N) and high bandwidth ($\approx 1$ kHz) to allow rapid characterization (to avoid reducing the thorax lifetime during testing). The comparison of empirical force data to simulated estimates showed that the quasi-steady state models still need much investigation to resolve the issue of which axis to measure the stroke angle and to account for wake capture. The estimates with ideally matched leading/lagging dynamics point to the need to using non-sinusoidal driving inputs in order to achieve reasonable thrust forces. The analysis also shows that there are numerous promising ways to increase the lift forces to

achieve MFI flight. For control purposes, a lookup table may be generated from the force map to solve the inverse dynamics problem, determining appropriate actuator input parameters (not necessarily unique) to provide desired body accelerations. This was not done because $02\theta$ is no longer functional and a more suitable force map to employ would not be based on amplitude variations in sinusoids.

## V. ACKNOWLEDGMENTS

## VI. REFERENCES

[1] S. Avadhanula, R.J. Wood, D. Campolo, and R.S. Fearing. Dynamically tuned design of the MFI thorax. In *Proc of IEEE Intl Conf on Robotics and Automation*, pages 52–9, Washington, DC, May 11-15 2002.

[2] A. Cox, D.J. Monopoli, M. Goldfarb, and E. Garcia. Development of piezoelectrically actuated micro-aerial vehicles. In *SPIE Microrobotics and Microassembly Symp*, pages 101–8, Boston, MA, Sept 1999.

[3] M.H. Dickinson, F-O. Lehmann, and S.P. Sane. Wing rotation and the aerodynamic basis of insect flight. *Science*, 284:1954–60, June 1999.

[4] R.C. Michelson and S. Reece. Update on flapping wing micro air vehicle research- Ongoing work to develop a flapping wing, crawling entomopter. In *Proc of 13th Bristol Intl RPV/UAV Systems Conf*, Bristol, UK, Mar 1998.

[5] T.N. Pornsin-Sirirak, S.W. Lee, H. Nassef, J. Grasmeyer, Y.C. Tai, C.M. Ho, and M. Keennon. MEMS wing technology for a battery-powered ornithopter. In *Proc. of IEEE 13th Annual Intl Conf on MEMS*, pages 799–804, Piscataway, NJ, Jan 2000.

[6] R. Ramamurti and W. Sandberg. Computational study of 3-D flapping foil flows. *39th AIAA Aerospace Sciences Meeting and Exhibit*, (AIAA-2001-0605), Jan 2001.

[7] S.P. Sane and M.H. Dickinson. The aerodynamic effects of wing rotation and a revised quasi-steady model of flapping flight. *J. Exp. Biol.*, 205:1087–96, 2002.

[8] L. Schenato, X. Deng, and S. Sastry. Virtual insect flight simulator (VIFS): A software testbed for insect flight,. In *Proc of IEEE Intl Conf on Robotics and Automation*, pages 3885–92, Seoul, Korea, May 21-36 2001.

[9] M. Sitti, D. Campolo, J. Yan, R.S. Fearing, T. Su, D. Taylor, and T.D. Sands. Development of PZT and PZN-PT based unimorph actuators for micromechanical flapping mechanisms. In *Proc of IEEE Intl Conf on Robotics and Automation*, pages 3839–46, Seoul, Korea, May 21-36 2001.

[10] R.J. Wood and R.S. Fearing. Flight force measurements for a micromechanical flying insect. In *IROS 2001*, Maui, HI, Oct 29-Nov 3 2001.

[11] J. Yan. *Design, Fabrication and Wing Force Control for a Micromechanical Flying Insect*. PhD thesis, University of California at Berkeley, 2002.

[12] J. Yan, R.J. Wood, S. Avadhanula, M. Sitti, and R.S. Fearing. Towards flapping wing control for a micromechanical flying insect. In *Proc of IEEE Intl Conf on Robotics and Automation*, pages 3901–8, Seoul, Korea, May 21-36 2001.